Radio Science, Volume 31, Number 4, Pages 931–941, July–August 1996

Subpicosecond electrodynamics of distributed Bragg reflector microlasers: Results from finite difference time domain simulations

Susan C. Hagness

Department of Electrical Engineering and Computer Science, McCormick School of Engineering and Applied Science, Northwestern University, Evanston, Illinois

Rose M. Joseph

Xerox Corporation, Webster, New York

Allen Taflove

Department of Electrical Engineering and Computer Science, McCormick School of Engineering and Applied Science, Northwestern University, Evanston, Illinois

Abstract. With advances in nanofabrication techniques leading to ever smaller and more intricate semiconductor laser structures, a detailed understanding of the electrodynamics of these micron-scale devices is required in order to optimize their design. The finite difference time domain (FD-TD) Maxwell's equations solver holds much promise for providing highly realistic simulations of novel microcavity lasers. We have extended the FD-TD algorithm to include the effects of frequency-dependent gain and gain saturation. This approach and its application to the modeling of distributed Bragg reflector microlasers is presented.

1. Introduction

Improvements in semiconductor fabrication technology have led to smaller and more complicated optical designs of lasers. Semiconductor lasers with physical dimensions of the order of the lasing wavelength, that is, microlasers, offer many attractive operating characteristics. For example, stimulated emission rates enhanced by low-dimensional photonic structures may permit terahertz modulation bandwidths. To bring this type of potential to reality, novel designs of device microstructures, such as microdisk [*McCall et al.*, 1992; *Chu et al.*, 1993] and photonic-wire microcavity [*Zhang et al.*, 1995] lasers, need to be further explored. Accurate modeling of the nonintuitive propagation and scattering behavior of such microlasers is an essential step in their development.

We have developed a computational tool that provides accurate modeling at the macroscopic level of the field dynamics in passive and active optical microcavities. Our approach is based on the finite difference time domain (FD-TD) method [*Taflove*, 1995], a computationally efficient numerical algorithm for the direct time integration of Maxwell's equations. FD-TD, originally developed to model electromagnetic interactions with arbitrary structures consisting of linear frequency-independent parameters, has recently been extended to frequency-dependent linear [*Joseph et al.*, 1991; *Luebbers and Hunsberger*, 1992] and nonlinear [*Goorjian and Taflove*, 1992; *Ziolkowski and Judkins*, 1993a] materials. With this advent, the range of mod-

Paper number 96RS00436.
0048-6604/96/96RS-00436$11.00

eling applications using FD-TD has been substantially expanded to include soliton propagation [*Goorjian et al.*, 1992; *Joseph et al.*, 1993; *Joseph and Taflove*, 1994] and self-focusing of light [*Ziolkowski and Judkins*, 1993b] in $\chi^{(3)}$ materials, pulse propagation through nonlinear corrugated waveguides [*Ziolkowski and Judkins*, 1994], and pulse-selective behavior in nonlinear Fabry-Perot cavities [*Basinger and Brady*, 1994]. To model distributed Bragg reflector (DBR) microlasers, we have chosen the FD-TD method, because it provides a complete electromagnetic analysis of arbitrary linear and nonlinear periodic structures; this level of analysis is most easily accessed with a full-wave time domain method. Furthermore, with the advanced state of computing power today, a complete FD-TD analysis of the electrodynamics of microlasers is indeed computationally feasible.

In this paper, we present an FD-TD formulation that permits the modeling of a saturable homogeneously broadened gain medium, where the linear gain profile is a single Lorentzian. In section 2, we describe our method for incorporating frequency-dependent linear gain and gain saturation into the standard FD-TD algorithm. The two generic validation studies presented in section 3 reveal the potential for high accuracy of the FD-TD model. The rest of the paper then focuses on the modeling of two different designs of microlasers: (1) Fabry-Perot surface-emitting lasers (FP-SELs) with vertical DBRs, and (2) novel photonic-wire microcavity lasers with in-plane photonic bandgap reflectors. In the first example, we compare uniform and periodic gain configurations within the cavity of the FP-SEL. Numerical results for the periodic gain structure show a substantial reduction in the material gain threshold, agreeing with experimental observations and analytical predictions of gain threshold reduction. In the second example, the passive characteristics of the photonic bandgap reflector are obtained. Using the standard FD-TD algorithm without gain, we present a cold-cavity analysis of the photonic-wire microcavity formed by two such reflectors.

2. FD-TD Algorithm

We consider a one-dimensional problem with electric and magnetic field components, E_z and H_y, propagating along the x direction through a nonmagnetic, isotropic medium. For the purpose of comparison to the algorithm for optical gain media, we first review the standard FD-TD algorithm, where field-material interactions are described by frequency-independent constants. In this case, Maxwell's curl equations in one dimension are

$$\frac{\partial H_y}{\partial t} = \frac{1}{\mu_o}\frac{\partial E_z}{\partial x}, \tag{1}$$

$$J_z + \epsilon\frac{\partial E_z}{\partial t} = \frac{\partial H_y}{\partial x}, \tag{2}$$

where $J_z = \sigma E_z$. Here the permittivity, ϵ, and the electric conductivity, σ, are independent of frequency. Using centered finite differences for the space and time derivatives, the curl equations can be expressed as second-order accurate finite difference equations:

$$H_y^{n+\frac{1}{2}}(i+\frac{1}{2}) = H_y^{n-\frac{1}{2}}(i+\frac{1}{2}) + \frac{\Delta t}{\mu_o \Delta x}[E_z^n(i+1) - E_z^n(i)], \tag{3}$$

$$E_z^{n+1}(i) = \frac{1-\frac{\sigma(i)\Delta t}{2\epsilon(i)}}{1+\frac{\sigma(i)\Delta t}{2\epsilon(i)}}E_z^n(i) + \frac{\frac{\Delta t}{\epsilon(i)\Delta x}}{1+\frac{\sigma(i)\Delta t}{2\epsilon(i)}}[H_y^{n+\frac{1}{2}}(i+\frac{1}{2}) - H_y^{n+\frac{1}{2}}(i-\frac{1}{2})]. \tag{4}$$

The vector field component $V_z^n(i)$ denotes sampling at space point $x = i\Delta x$ and time point $t = n\Delta t$. To obtain the solution for the field components, the two-step recursive process is iterated to the desired final observation time.

Two different methods for incorporating linear gain into the FD-TD model have recently been demonstrated. *Hawkins and Kallman* [1994] simulated gain as a frequency-dependent susceptibility. Their method is based on well-known

approaches for modeling linear dispersion; they demonstrated that an appropriate choice of dispersion parameters produces the effect of gain. Our group [*Hagness and Taflove*, 1994] simultaneously developed the method described below, which covers linear as well as nonlinear gain. Here gain is incorporated as a frequency-dependent conductivity. To illustrate this method, we consider a homogeneously broadened gain medium. In this case, the atoms of the gain medium are indistinguishable and have the same atomic transition frequency, ω_o. (See *Yariv* [1989], for example, for a more detailed physical explanation.) Therefore the small-signal linear gain coefficient is governed by a single Lorentzian profile. The gain coefficient should also include the large-signal nonlinear effect of saturation, which is due to the decrease of the population inversion with field intensity. Accordingly, we express the frequency-dependent conductivity as

$$\sigma(\omega) = \frac{\mathcal{J}_z(\omega)}{\mathcal{E}_z(\omega)} \tag{5}$$
$$= \frac{1}{1+\frac{I}{I_s}}\left[\frac{\sigma_o/2}{1+j(\omega-\omega_o)T_2}+\frac{\sigma_o/2}{1+j(\omega+\omega_o)T_2}\right],$$

using Hermitian symmetry for the Lorentzian. Here σ_o is related to the peak value of the gain set by the pumping level, T_2 is the dipole relaxation time, and I_s is the saturation intensity.

To see how this gives gain, consider the linear case when the intensity, I, is small compared to the saturation intensity, I_s. The expression for $\sigma(\omega)$ simplifies and can be separated into real and imaginary parts,

$$\begin{aligned}\sigma(\omega) &= \sigma_R(\omega) + j\,\sigma_I(\omega)\\ &= \frac{\sigma_o\left[1+(\omega_o^2+\omega^2)T_2^2\right]}{\left[1+(\omega_o^2-\omega^2)T_2^2\right]^2+4\omega^2T_2^2}\\ &+ j\frac{\sigma_o\omega T_2\left[-1+(\omega_o^2-\omega^2)T_2^2\right]}{\left[1+(\omega_o^2-\omega^2)T_2^2\right]^2+4\omega^2T_2^2}.\end{aligned} \tag{6}$$

From the homogeneous wave equation for a plane wave in this medium, we see that upon assuming the form $E_z(x,t) = \mathcal{E}_z(x,\omega)e^{-j\omega t}$,

$$\nabla^2\mathcal{E}_z + \frac{\omega^2}{c^2}\left(\tilde{\epsilon_r}(\omega) + j\,\frac{\sigma_R(\omega)}{\omega\epsilon_o}\right)\mathcal{E}_z = 0, \tag{7}$$

where the effective permittivity, given by $\tilde{\epsilon_r}(\omega) \equiv \epsilon_r - \sigma_I(\omega)/\omega\epsilon_o$, depends on frequency. We further see that upon assuming the form $\mathcal{E}_z(x,\omega) = \mathcal{E}_o e^{jk_c x}$,

$$k_c^2 = \frac{\omega^2}{c^2}\left(\tilde{\epsilon_r}(\omega) + j\,\frac{\sigma_R(\omega)}{\omega\epsilon_o}\right). \tag{8}$$

The complex wave number, k_c, may be separated into real and imaginary parts: $k_c = \beta + j\,\alpha$. The exponential propagation factor, e^{jk_cx}, then becomes $e^{j\beta x}e^{-\alpha x}$. The term $e^{-\alpha z}$ in this expression acts as an amplifier when α is negative. The expressions for α and β, however, are somewhat complicated; they can be simplified by making the reasonable assumption that $\sigma_R(\omega)/\omega\epsilon_o\tilde{\epsilon_r}(\omega) \ll 1$, that is, the material is low-gain. In this case,

$$\alpha(\omega) \simeq \sigma_R(\omega)/2c\epsilon_o\tilde{n}, \tag{9}$$
$$\beta(\omega) \simeq \tilde{n}\omega/c, \tag{10}$$

where $\tilde{n} = \sqrt{\tilde{\epsilon_r}}$. From (9), we conclude that if $\sigma_R(\omega)$ is negative, then α is negative, providing gain. According to (6), this is the case when the parameter σ_o is chosen to be negative.

As an initial step, we have developed the following algorithm by assuming that the saturation intensity is a constant parameter rather than a function of frequency. Also, we treat the spatially dependent intensity, $I = \frac{1}{2}cn\epsilon_o\mathcal{E}_o$, as a feedback parameter in time. Taking the inverse Fourier transform of (5) provides the following auxiliary differential equation that can by solved simultaneously with (2):

$$(1+\omega_o^2T_2^2)J_z + 2T_2\frac{\partial J_z}{\partial t} + T_2^2\frac{\partial^2 J_z}{\partial t^2} = s\sigma_oE_z + s\sigma_oT_2\frac{\partial E_z}{\partial t}. \tag{11}$$

Here $s \equiv \frac{1}{1+I/I_s}$ is the saturation coefficient that contains feedback information of the latest peak electric field. With the goal of implementing a central differencing procedure of (2) and (11) at

time step $n+\frac{1}{2}$, we define an auxiliary variable, F_z, and rewrite (11) as two first-order differential equations:

$$F_z \equiv \frac{\partial J_z}{\partial t}, \tag{12}$$

$$(1+\omega_o^2 T_2^2)J_z + 2T_2 F_z + T_2^2 \frac{\partial F_z}{\partial t} = s\sigma_o E_z + s\sigma_o T_2 \frac{\partial E_z}{\partial t}. \tag{13}$$

We next set up three finite difference expressions for the system of differential equations (2), (12), and (13) at time step $n+\frac{1}{2}$. Solving the resulting system of finite difference expressions for the three unknowns $F_z^{n+1}(i)$, $J_z^{n+1}(i)$, and $E_z^{n+1}(i)$ yields the following explicit expressions:

$$F_z^{n+1}(i) = A_1[H_y^{n+\frac{1}{2}}(i+\frac{1}{2}) - H_y^{n+\frac{1}{2}}(i-\frac{1}{2})] + A_2 E_z^n(i) + A_3 J_z^n(i) + A_4 F_z^n(i), \tag{14}$$

$$J_z^{n+1}(i) = J_z^n(i) + \frac{\Delta t}{2}[F_z^{n+1}(i) + F_z^n(i)], \tag{15}$$

$$E_z^{n+1}(i) = E_z^n(i) - \frac{\Delta t}{2\epsilon}[J_z^{n+1}(i) + J_z^n(i)] + \frac{\Delta t}{\epsilon \Delta x}[H_y^{n+\frac{1}{2}}(i+\frac{1}{2}) - H_y^{n+\frac{1}{2}}(i-\frac{1}{2})], \tag{16}$$

where

$$A_1 = \frac{4\Delta t\, s(i)\, \sigma_o(\Delta t + 2T_2)}{\Delta x\, \beta}, \quad A_2 = \frac{8\epsilon\, s(i)\, \sigma_o \Delta t}{\beta},$$

$$A_3 = -\frac{4\Delta t[2\epsilon(1+\omega_o^2 T_2^2) + s(i)\,\sigma_o(\Delta t + 2T_2)]}{\beta},$$

$$A_4 = -\frac{8\epsilon\, T_2(\Delta t - T_2)}{\beta} - \frac{(\Delta t)^2[2\epsilon(1+\omega_o^2 T_2^2) + s(i)\,\sigma_o(\Delta t + 2T_2)]}{\beta},$$

$$\beta = 8\epsilon\, T_2(\Delta t + T_2) + (\Delta t)^2[2\epsilon(1+\omega_o^2 T_2^2) + s(i)\,\sigma_o(\Delta t + 2T_2)],$$

$$s(i) = \frac{1}{1+\frac{I(i)}{I_s}}, \quad I(i) = \frac{1}{2} cn\epsilon_o [E_z^{\text{peak}}(i)]^2. \tag{17}$$

For a linear medium, there is no feedback; the saturation coefficient reduces to $s = 1$, because the intensity is negligible compared to the saturation intensity. For a nonlinear medium, the saturation coefficient is updated as follows. If the electric field at time step n is greater than the electric field at time step $n-1$ at the same location in space, then the saturation coefficient is updated, using $E_z^{\text{peak}}(i) = E_z^n(i)$. On the other hand, if the electric field at time step n has decreased from its previous value, then the saturation coefficient is not updated; hence $s(i)$ remains based on the latest peak electric field. In this manner, intensity feedback in the time domain retains as much as possible its frequency domain meaning. Note that since the feedback is performed independently at each grid location, we are simulating a spatially inhomogeneously broadened medium in which spatial hole burning may occur.

Equations (3), (14), (15), and (16) compose the complete FD-TD time-stepping algorithm for the single Lorentzian optical gain medium using the auxiliary differential equation approach. The computational model is now a four-step recursive process that retains the fully explicit nature of the original frequency-independent FD-TD algorithm and requires storage of fields only one step back in time. It is easily extended to arbitrary two- and three-dimensional problems with heterogeneous media.

3. Validations

We demonstrate the accuracy of this method with two validation studies. In the first study, the accuracy of the FD-TD algorithm for linear frequency-dependent gain is tested. The electric field propagation factor, defined by $e^{jk_c(x_2-x_1)} = \mathcal{E}_z(x_2,\omega)/\mathcal{E}_z(x_1,\omega)$, is computed for a linear gain medium with $\lambda_o = 0.89$ μm, $T_2 = 0.07$ ps, and $n = 3.59$. As a single Gaussian pulse with a 5-fs temporal width between the $1/e$ points and a carrier frequency of ω_o propagates through the medium, data are taken every time step at two fixed observation points separated by a distance of $l = x_2 - x_1 = \lambda_o/n$. By taking the ratio of the discrete Fourier transforms of the pulses at the two locations, the complex-valued propagation factor from the FD-TD model is calculated over the full bandwidth of the pulse, which is 60 times the 5 THz bandwidth of the gain spectrum. In

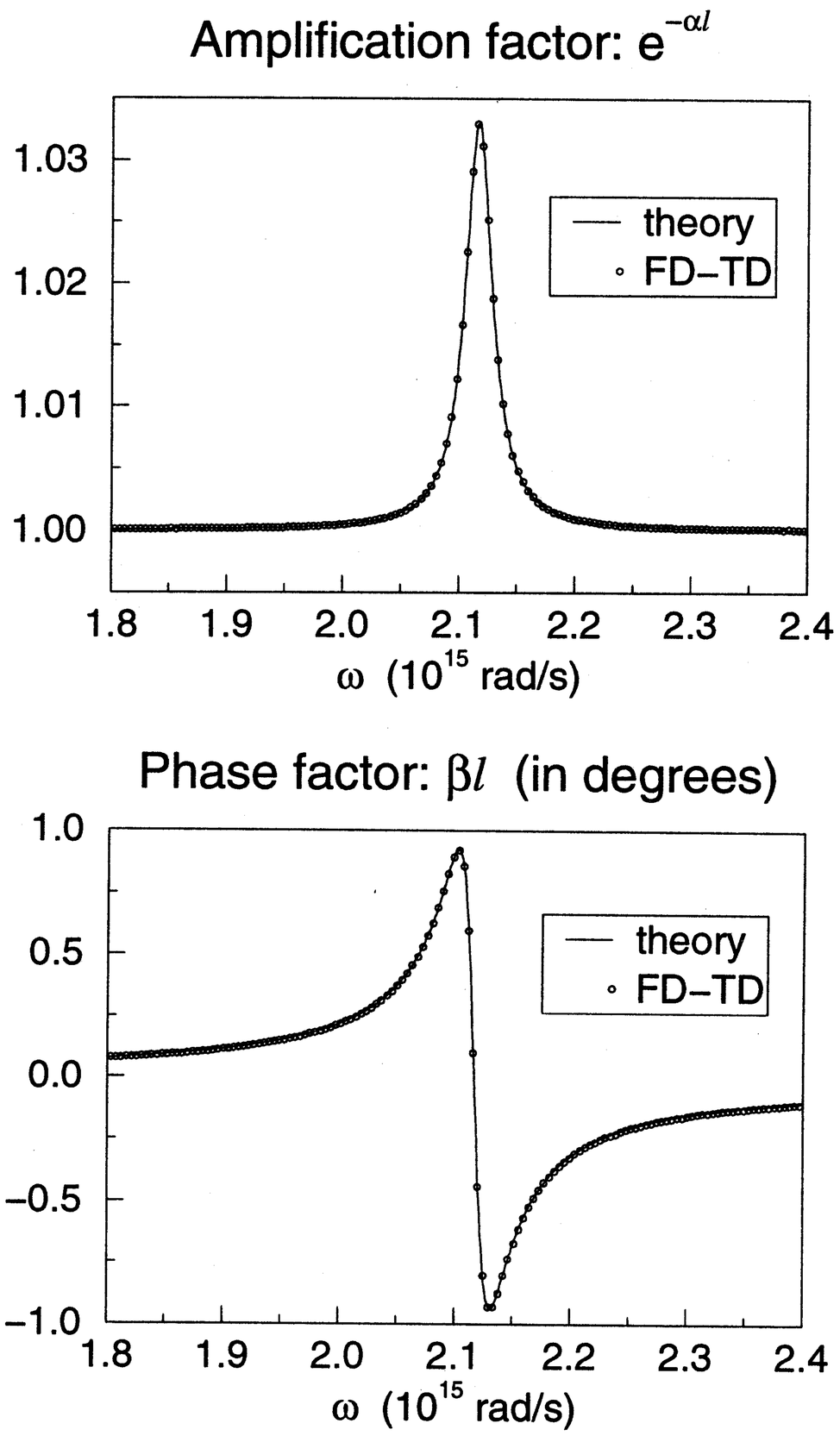

Figure 1. Comparison of finite difference time domain (FD-TD) results and theory for the amplification and phase factors of a pulse propagating a distance of one dielectric wavelength in a linear gain medium with $\sigma_o = -5000$ mho/m.

Figure 1, the amplification factor, $e^{-\alpha l}$, and the phase of the propagation factor, βl, corrected by the amount $n\omega l/c$ to give the phase due solely to the presence of gain, are compared with the exact profiles. At a very fine grid resolution of $\Delta x = \lambda_o/400n = 0.62$ nm ($\Delta t = 0.002068$ fs), the deviation from the exact values over the complete frequency range is less than 2 parts per 10,000 in the amplification factor and less than 0.006° in the phase factor. This indicates the validity and potential for high accuracy of the FD-TD model over extremely large instantaneous bandwidths.

In the second study, the FD-TD algorithm for frequency-dependent gain and gain saturation is applied to a one-dimensional Fabry-Perot etalon, the simplest geometry for a laser oscillator. The following parameters chosen for the gain medium correspond to GaAs: $\lambda_o = 0.89$ μm, $T_2 = 0.07$ ps, $n = 3.59$, and $I_s = 65.2$ kW/cm^2. The cavity, filled entirely with gain medium, has a length $l = 12.4$ μm. The mirrors at each end of the cavity are formed by the interface between the semiconductor gain medium and air; the reflectivity, R, of each end facet is independent of frequency. For a cavity with no internal loss, the material gain required at threshold is given by $\alpha_{\text{th}} = \frac{1}{2l} \ln R$. We use (9) to determine the threshold value of σ_o for which $\alpha(\omega_o) = \alpha_{\text{th}}$. From the laser parameters listed above, the approximate theoretical value of $\sigma_{o_{\text{th}}}$ is -1760 mho/m. Figure 2 shows the unsaturated gain curve for an above-threshold choice of σ_o. The cavity resonances are marked by the vertical lines; for $\sigma_o = -7000$ mho/m, three longitudinal modes $(\omega_{m-1}, \omega_m, \omega_{m+1})$ lie in the region where the unsaturated gain exceeds the round-trip loss. Since this is a homogeneously broadened system, we expect the longitudinal mode with the highest unsaturated

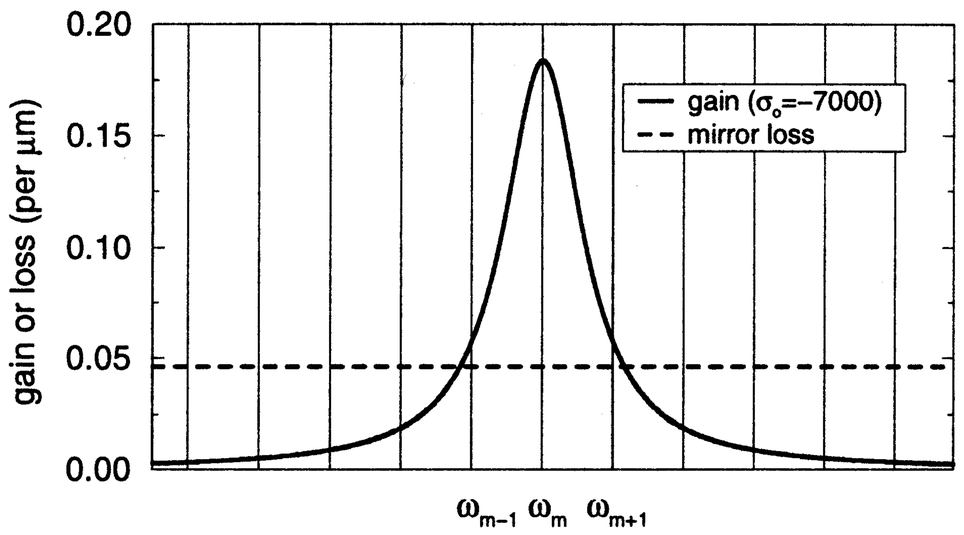

Figure 2. Unsaturated gain and loss spectra for a Fabry-Perot etalon with gain. The longitudinal modes of the Fabry-Perot cavity are shown as vertical lines.

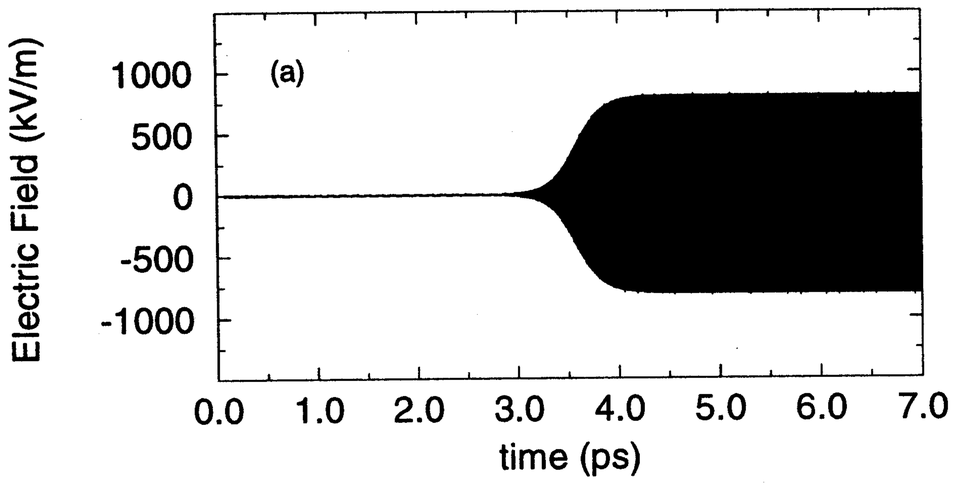

Figure 3. (a) FD-TD simulation of the time-varying electric field outside the Fabry-Perot laser cavity. (b) Expanded timescale of the steady state region showing single-mode oscillation at ω_o.

gain to clamp the gain curve at the loss line, yielding single-mode operation. In this example, the frequency of the lasing mode is designed to be $\omega_m = \omega_o$, that is, the peak of the gain curve.

The FD-TD results for the second study are shown in Figures 3 and 4. Within a semiclassical framework, spontaneous emission can be included in Maxwell's equations as a noise current [*Agrawal and Dutta*, 1993]. We have used a pseudorandom number generator for zero-mean white Gaussian noise to implement the noise current inside the laser cavity. The FD-TD computed time evolution of the electric field outside the laser cavity is shown in Figure 3. In Figure 3a, the transient response is shown; the electric field oscillations build up rapidly after a delay, then saturate as the gain saturates. Figure 3b shows an expanded timescale of the steady state region of Figure 3a, which illustrates that the FD-TD model correctly predicts a lasing frequency of ω_o. This simulation, performed for $\sigma_o = -7000$ mho/m, was repeated for smaller values of σ_o. In each simulation, the output intensity was computed from the steady state data. The results, plotted as a light-current (L-I) curve in Figure 4, show that the output intensity varies linearly with the above-threshold gain level. This is expected for a homogeneously broadened system. Furthermore, the FD-TD simulations provide an accurate estimate of the gain threshold. By extrapolating the data in Figure 4, we obtained an estimate of $\sigma_{o_{\text{th}}} \simeq -1780$ mho/m, which corresponds closely to the value calculated above.

4. Results for Surface-Emitting Laser With Periodic Gain

Over the past several years, SELs have been intensively studied for their many advantages. By employing extremely short cavity lengths and high-reflectivity DBR mirrors, the SEL exhibits improved lasing characteristics, that is, remarkably low thresholds, high output powers, and single-mode operation. It is well known that the lasing threshold of an SEL can be further improved using a periodic gain active structure. By placing thin gain segments along the electric field standing wave maxima, the longitudinal confinement factor, Γ, is maximized. *Corzine et al.* [1989] developed an analytical method for

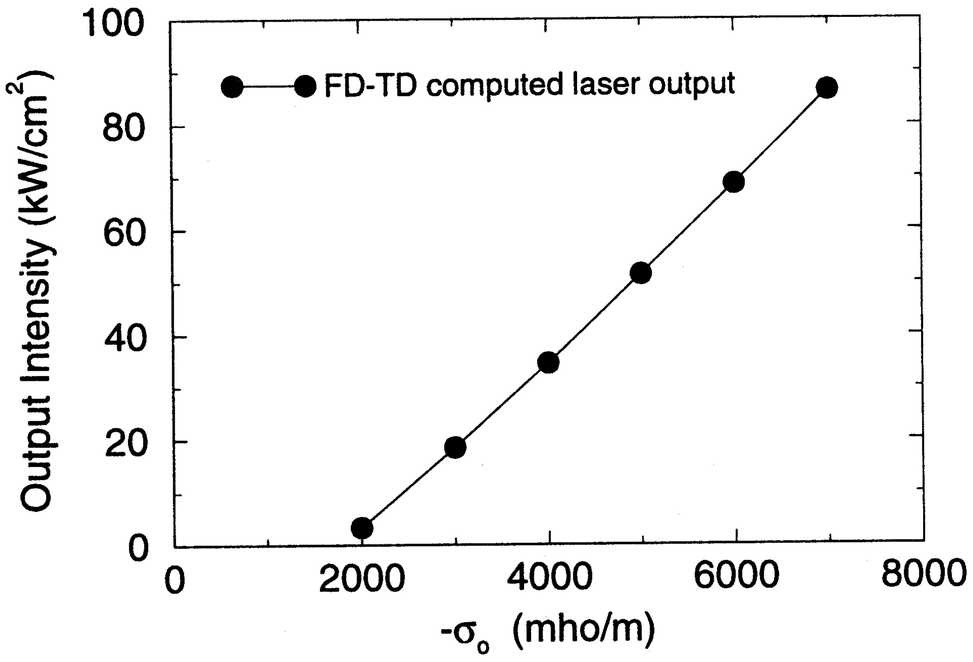

Figure 4. FD-TD computed light-current (L-I) curve for the output intensity of the Fabry-Perot laser.

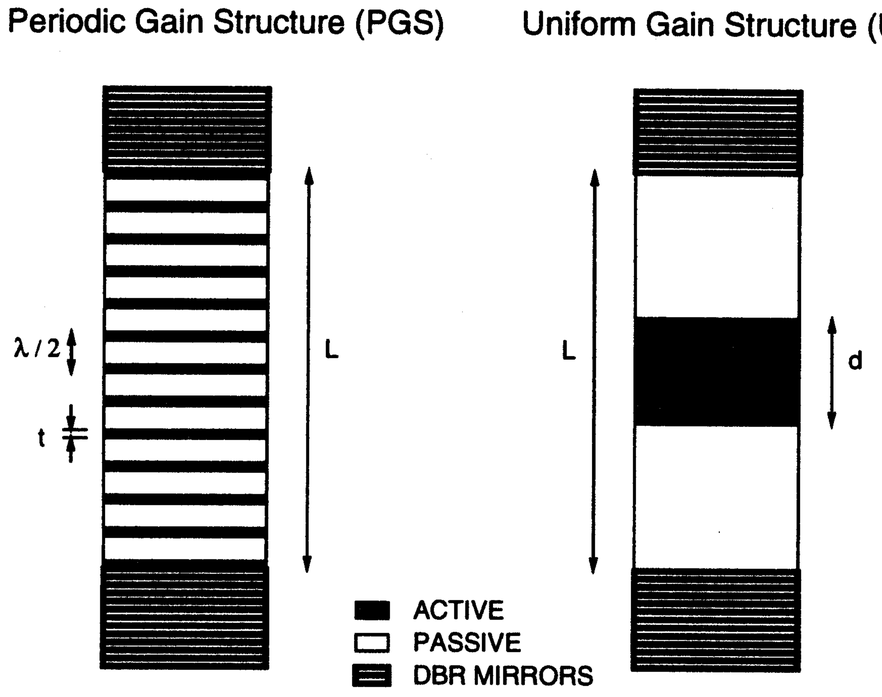

Figure 5. Schematic of microcavity Fabry-Perot surface-emitting lasers (FP-SELs) with vertical distributed Bragg reflectors (DBRs) and uniform (UGS) and periodic gain structures (PGS) within the cavity.

optimizing the design of the periodic gain structure. They demonstrated that close to a factor of 2 reduction in the material gain threshold is possible.

In this section, we use the FD-TD algorithm described in section 2 to model one-dimensional microcavity FP-SELs with uniform and periodic gain structures (UGS and PGS), shown in Figure 5. The mirrors for each microlaser are $Al_{0.2}Ga_{0.8}As/AlAs$ DBRs with a Bragg wavelength of $\lambda_B = 0.87\ \mu m$; the top mirror uses nine pairs and the bottom mirror uses 12.5 pairs. Both the active and passive regions of the cavity, as well as the substrate, are made of GaAs. The indices of refraction for this microlaser are as follows: $n(\mathrm{GaAs}) = 3.59$, $n_H(Al_{0.2}Ga_{0.8}As) = 3.45164$, $n_L(\mathrm{AlAs}) = 2.971$, and $n(\mathrm{air}) = 1.0$. Each cavity has a length $L = 27\ \lambda_B/2$. The cavity for the UGS consists of a solid active GaAs region of length d surrounded on each side by a passive GaAs region. The cavity for the PGS consists of thin active GaAs segments, each with a thickness t, separated by passive GaAs segments; the total length of the gain segments is equal to d. The fill factor, defined as d/L, was chosen to be 0.5. Once the lasing wavelength of the UGS is determined, the PGS design can be completed using a spacing of $\lambda_{laser}/2$ between the gain segments. We chose these design parameters in order to be able to compare our numerical results with the analysis presented by *Corzine et al.* [1989]. The relevent analytical expressions are listed here. For a cavity with no internal loss, the material gain required at threshold is given by $\alpha_{th} = \frac{1}{\Gamma}\frac{1}{2L}\ln R$, where R is the geometric mean mirror reflectivity. For the UGS, the longitudinal confinement factor is simply the fill factor: $\Gamma_{UGS} = d/L$. Assuming a uniform standing wave pattern and ideal mirror reflectivities, the longitudinal confinement factor for the PGS can be approximated as

$$\Gamma_{PGS} = \frac{d}{L}\left\{1 + \frac{\sin[\pi(\frac{t}{\lambda/2})]}{\pi(\frac{t}{\lambda/2})}\right\}, \qquad (18)$$

where λ is the lasing wavelength. When $t = \lambda/2$, the confinement factor for the PGS reduces to that of the UGS. When $t = 0$, that is, when the gain segments are extremely thin, the confinement factor is maximized at twice that of the UGS. Hence we see the potential reduction in the gain threshold by a factor of 2.

We first used the standard FD-TD method, without gain, to determine the passive characteristics of the microlaser. In this case, the UGS and PGS are identical when the gain is turned off, because the refractive indices of the passive and active regions are the same. For each of the mirrors, we computed the reflectivity spectrum with a single FD-TD run, using a short-pulse excitation and a discrete Fourier transformation of the time domain data. In Figure

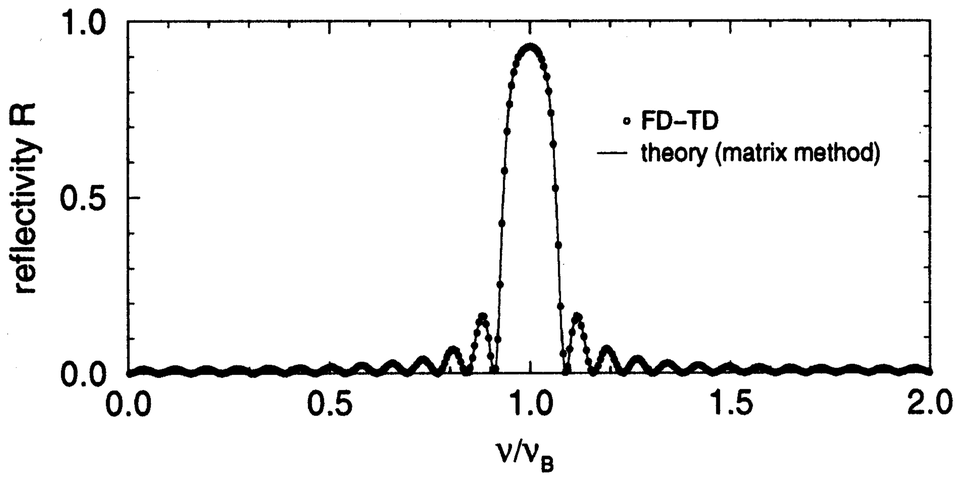

Figure 6. FD-TD computed reflectivity spectrum for the bottom mirror of the microcavity FP-SEL.

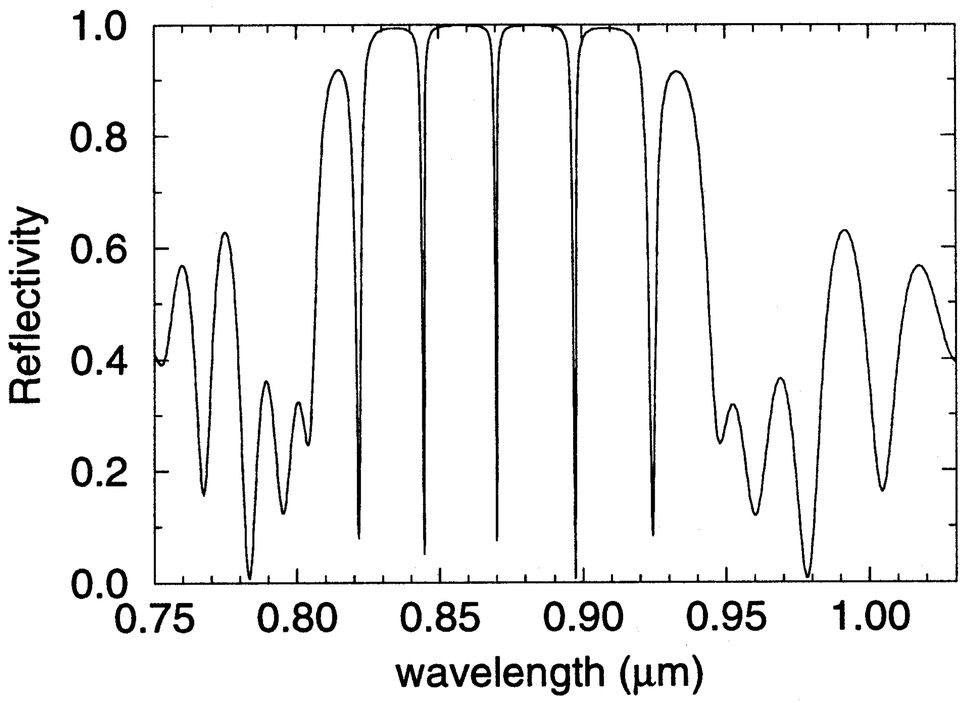

Figure 7. FD-TD computed reflectivity spectrum for the entire microcavity FP-SEL. The gain regions are inactive for this cold-cavity analysis.

6, the FD-TD results for the bottom DBR are compared with the analytical spectrum given by the matrix method. At a grid resolution of $\Delta x = \lambda_B/124n_H = 2.033$ nm ($\Delta t = 0.00678$ fs), the deviation from the matrix method at the reflectivity peak is less than 3 parts per 10,000. Similar results are obtained for the top mirror. We determined the cold-cavity resonant modes by computing the reflectivity spectrum of the entire structure (cavity and mirrors). In Figure 7, five resonances are evident within the broad stopband. With knowledge of the spacing between the effective resonant frequencies, one can determine the effective cavity length, which differs from the physical length because of field penetration into the mirrors. In this case, the effective cavity length is approximately 34 half Bragg wavelengths, compared to the physical length of 27 half Bragg wavelengths. Since the gain peak of GaAs is at $\lambda = 0.89$ μm and the gain bandwidth is narrower than the reflectivity bandwidth of the mirrors, the first effective resonant wavelength to the right of the Bragg wavelength will experience the greatest net gain; therefore the lasing wavelength should be close to 0.897 μm rather than 0.87 μm.

We then used the FD-TD algorithm for gain to determine the lasing wavelength and gain threshold for the UGS and PGS. The gain parameters for the active regions are those corresponding to GaAs. Following the methodology presented in the second study of section 3, we determined the lasing wavelength for the microcavity FP-SEL with a UGS by looking at the steady state data for the electric field outside the top mirror. The lasing wavelength in our numerical simulation is just under 0.9 μm, as predicted. The FD-TD results for the steady state electric field distribution throughout the UGS are shown in Figure 8. The decaying fields on either side of the cavity illustrate the penetration of the mode into the passive mirrors. The standing wave maxima within the cavity, spaced periodically by $\lambda_{laser}/2$, determine the locations

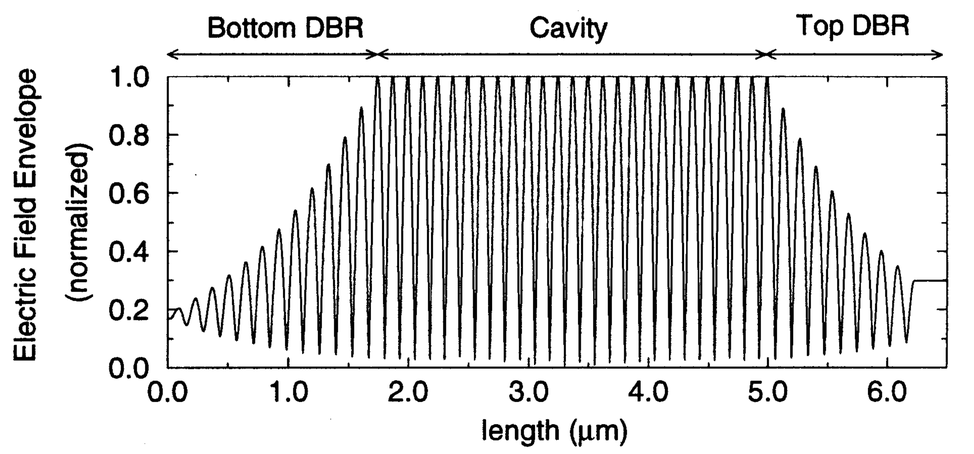

Figure 8. FD-TD results for the spatially varying steady state electric field pattern throughout the microcavity FP-SEL with a UGS.

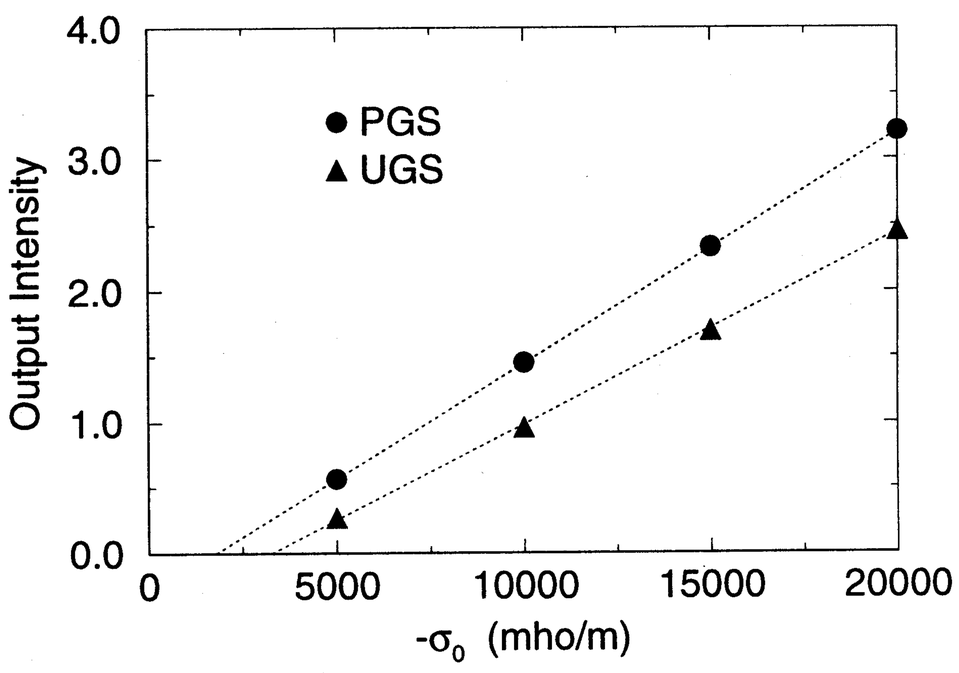

Figure 9. FD-TD computed L-I curve for the output intensity of the the microcavity FP-SEL. Comparison between the UGS and PGS reveals the following advantages of the PGS: a substantial reduction in gain threshold and a higher output intensity.

for the thin gain segments in the PGS. For each structure, the simulation is repeated for different values of σ_o; the resulting L-I curves are shown in Figure 9. Extrapolation of the data yields a gain threshold of $\sigma_{o_{\text{th}}} \simeq -3260$ mho/m for the UGS and a gain threshold of $\sigma_{o_{\text{th}}} \simeq -1790$ mho/m for the PGS. Thus our FD-TD simulations indicate that the gain threshold for the PGS is approximately 45% less than the gain threshold for the UGS. The approximate analytical expression (18) for the PGS suggests that the gain threshold for the PGS is 38.5% less than the gain threshold for the UGS.

5. Results for Photonic-Wire Microcavity

Periodic spatial variation in the linear dielectric constant of a device can result in a photonic band structure analogous to the electronic bandgap in semiconductor materials. The periodicity gives rise to variations in reflection and transmission characteristics. Of particular interest are frequency stopbands over which there is no transmission. Analysis of such lattice structures usually involves the assumption that the lattice is infinite, allowing the wave equation to be expanded in plane waves and solved using eigenvalue techniques [*Plihal and Maradudin*, 1991]. The standard FD-TD algorithm without gain treats passive finite photonic bandgap structures (PBS) in a straightforward manner; this method has been used successfully to model a two-dimensional array at microwave frequencies [*Kelly et al.*, 1994], giving good results for transmission and reflection profiles for both transverse electric (TE) and transverse magnetic polarizations.

In this section, we consider a strongly guiding optical waveguide as the basis of a microcavity laser. Such a waveguide is called a photonic wire if a high percentage of spontaneous emission is channeled into the lowest-order guided mode. It has been shown that a photonic-wire laser can have a spontaneous emission coupling efficiency as high as 35% [*Zhang et al.*, 1995], yielding a low lasing threshold. The waveguide we consider here is composed of a high-refractive index semiconductor core ($n = 3.4$) surrounded by a low-refractive index cladding ($n = 1$). Finite PBS consisting of one-dimensional arrays of holes can be used as very broadband DBRs to define the laser cavity. Using nanofabrication techniques [*Zhang et al.*, 1996], arrays of air holes are etched in the semiconductor guiding layer, periodically spaced along the guide (Figure 10).

A 0.3-μm-wide photonic wire with five rectangular holes is modeled with a uniform spatial resolution of 0.0125 μm in two dimensions ($\Delta t =$ 0.02085 fs). The holes are 0.25 μm $\times$ 0.1 μm, and the spacing between them is 0.225 μm. In this two-dimensional representation, the waveguide is modeled as an infinite slab in the vertical direction; the height of the holes is assumed unbounded. In order to obtain broadband spectral information with a single FD-TD computer run, a short TE-polarized optical pulse (full width at half maximum is 30 fs, $\lambda_0 = 1.5$ μm) is excited at the left end of the waveguide and allowed to propagate to the right. The waveguide and the grid boundaries are terminated using the Berenger perfectly matched layer absorbing

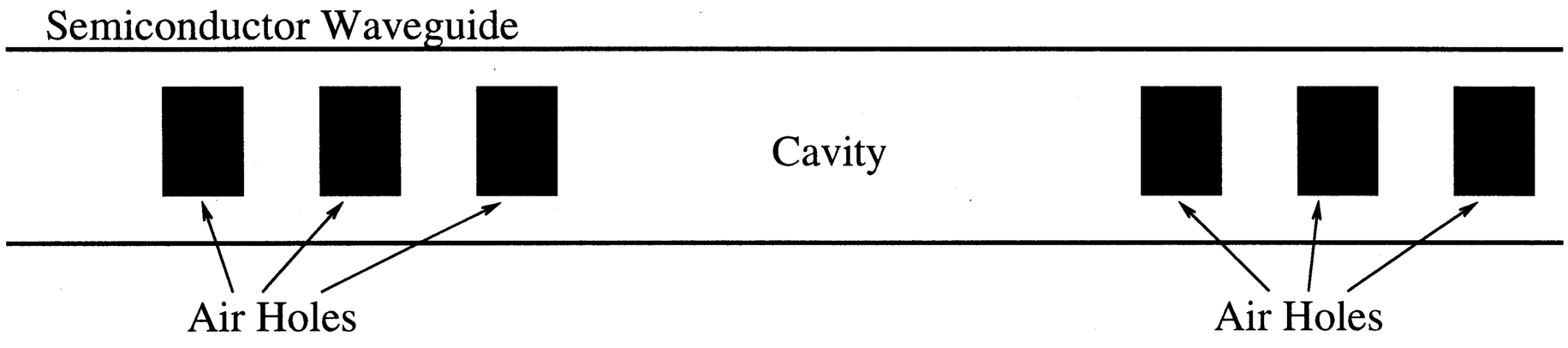

Figure 10. Schematic of a photonic-wire laser cavity defined by two photonic bandgap structures which act as broadband DBRs.

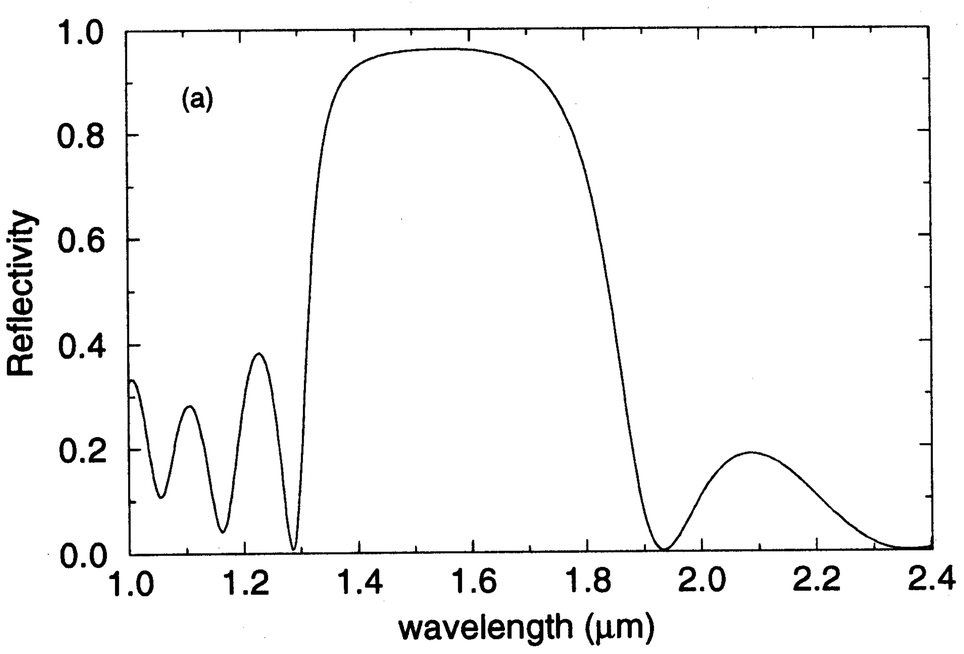

Figure 11. FD-TD computed reflectivity spectra for (a) a single photonic bandgap reflector composed of five periodically spaced air holes ($\lambda_B = 1.55$ μm), and (b) a photonic-wire microcavity composed of two photonic bandgap reflectors separated by a length of 0.525 μm.

boundary condition [*Taflove*, 1995]. Reflection and transmission spectra can be obtained from the time domain data via discrete Fourier transform. The run times on a CRAY C90 (single processor) were 60 s for the single PBS and 2100 s for the entire cavity.

The reflection profile of a single PBS computed using our method is given in Figure 11a. With only five holes, the photonic bandgap mirror gives a reflectivity bandwidth greater than 300 nm and a peak reflectivity higher than 95%. Using the multilayer DBRs common in vertical-cavity SELs, many more layers would be required to achieve an equivalently high peak reflectivity. Figure 11b shows the computed reflection profile of the entire photonic-wire microcavity, consisting of a photonic bandgap reflector, a section of waveguide, followed by a second photonic bandgap reflector. The distance between reflectors in this case is 0.525 μm; the effective cavity length is slightly longer because of the distributed nature of the reflectors. Since the cavity length is so small, there is only one resonant mode ($\lambda = 1.6$ μm) within the reflectivity stopband. This resonance gives us an estimate of the quality factor (Q) of the microcavity. From Figure 11b, we have estimated that $Q \simeq 300$. By changing the size, shape, spacing, and number of holes in our simulations, we are able to customize the design of the microlaser for specific applications.

6. Conclusions and Future Work

In this paper, we have presented a formulation for including frequency-dependent gain with saturation in FD-TD simulations. We have shown that our approach accurately models the amplification of a broadband electromagnetic pulse in an optical gain medium described by a single Lorentzian profile. Our simulation of a simple Fabry-Perot laser demonstrates the validity of this method for providing accurate predictions of the gain threshold and the lasing wavelength. Furthermore, we have shown that our method provides accurate one-dimensional modeling of Fabry-Perot surface-emitting DBR microlasers with PGS within the cavity. The algorithm presented here is easily extended to complicated two- and three-dimensional problems. More complicated gain spectra can be approximated by using a linear combination of Lorentzians.

We have found that the FD-TD method is essential for optimizing the design of novel microstructures, such as the photonic-wire microlaser. We are currently conducting three-dimensional simulations of the photonic-wire microcavity, taking into account the finite heights of the holes composing the photonic bandgap reflectors. The three-dimensional model takes into account the vertical diffraction effects in the hole region, allowing us to fully optimize the design by minimizing the amount of diffraction loss.

In summary, we believe this approach has the potential to serve as a practical engineering tool for providing reliable simulations on a phenomenological level of the full-wave electrodynamics of complicated micron-scale lasers, where reflections and coherent effects are significant.

Acknowledgments. This research was supported in part by ONR contract N00014-93-0133, NSF grant ECS-9218494, and Cray Research, Inc. We would like to thank S. T. Ho at Northwestern University for experimental collaborations.

References

Agrawal, G. P., and N. K. Dutta, *Semiconductor Lasers,* 2nd ed., p. 235, Van Nostrand Reinhold, New York, 1993.

Basinger, S. A., and D. J. Brady, Finite-difference time-domain modeling of dispersive nonlinear Fabry-Perot cavities, *J. Opt. Soc. Am. B Opt. Phys.*, *11*(8), 1504–1511, 1994.

Chu, D. Y., M. K. Chin, N. J. Sauer, Z. Xu, T. Y. Chang, and S. T. Ho, 1.5-μm InGaAs/InAlGaAs quantum-well microdisk lasers, *IEEE Photonics Technol. Lett.*, *5*(12), 1353–1355, 1993.

Corzine, S. W., R. S. Geels, J. W. Scott, R. H. Yan, and L. A. Coldren, Design of Fabry-Perot surface-emitting lasers with a periodic gain structure, *IEEE J. Quantum Electron.*, *25*(6), 1513–1524, 1989.

Goorjian, P. M., and A. Taflove, Direct time integration of Maxwell's equations in nonlinear dispersive media for propagation and scattering of femtosecond electromagnetic solitons, *Opt. Lett.*, *17*(3), 180–182, 1992.

Goorjian, P. M., A. Taflove, R. M. Joseph, and S. C. Hagness, Computational modeling of femtosecond optical solitons from Maxwell's equations, *IEEE J. Quantum Electron.*, *28*(10), 2416–2422, 1992.

Hagness, S. C., and A. Taflove, A nonlinear full-wave electromagnetic model of semiconductor laser cavities, paper presented at *Optical Society of America Annual Meeting*, Opt. Soc. of Am., Dallas, Tex., October 1994.

Hawkins, R. J., and J. S. Kallman, Lasing in tilted-waveguide semiconductor laser amplifiers, *Opt. Quantum Electron.*, *26*, S207–S217, 1994.

Joseph, R. M., and A. Taflove, Spatial soliton deflection mechanism indicated by FD-TD Maxwell's equations modeling, *IEEE Photonics Technol. Lett.*, *6*(10), 1251–1254, 1994.

Joseph, R. M., S. C. Hagness, and A. Taflove, Direct time integration of Maxwell's equations in linear dispersive media with absorption for scattering and propagation of femtosecond electromagnetic pulses, *Opt. Lett.*, *16*(18), 1412–1414, 1991.

Joseph, R. M., P. M. Goorjian, and A. Taflove, Direct time integration of Maxwell's equations in two-dimensional dielectric waveguides for propagation and scattering of femtosecond electromagnetic solitons, *Opt. Lett.*, *18*(7), 491–493, 1993.

Kelly, P. K., J. G. Maloney, B. L. Shirley, and R. L. Moore, Photonic band structures of finite thickness: Theory and experiment, paper presented at *IEEE Antennas and Propagation Society International Symposium*, Inst. of Electr. and Electron. Eng., Seattle, Wash., June 1994.

Luebbers, R. J., and F. Hunsberger, FDTD for Nth-order dispersive media, *IEEE Trans. Antennas Propag.*, *40* (11), 1297–1301, 1992.

McCall, S. L., A. F. J. Levi, R. E. Slusher, S. J. Pearton, and R. A. Logan, Whispering-gallery mode microdisk lasers, *Appl. Phys. Lett.*, *60*(3), 289–291, 1992.

Plihal, M., and A. A. Maradudin, Photonic band-structure of two-dimensional systems: The triangular lattice, *Phys. Review B Condens. Matter*, *44*(16), 8565–8571, 1991.

Taflove, A., *Computational Electrodynamics: The Finite-Difference Time-Domain Method*, Artech House, Boston, 1995.

Yariv, A., *Quantum Electronics,* 3rd ed., John Wiley, New York, 1989.

Zhang, J. P., D. Y. Chu, S. L. Wu, S. T. Ho, W. G. Bi, C. W. Tu, and R. C. Tiberio, Photonic-wire laser, *Phys. Rev. Lett.*, *75*(14), 2678-2681, 1995.

Zhang, J. P., D. Y. Chu, S. L. Wu, R. M. Joseph, A. Taflove, S. T. Ho, W. G. Bi, C. W. Tu, and R. C. Tiberio, Nanofabrication of 1-D photonic-bandgap and photonic-wire structure, *IEEE Photonics Technol. Lett.*, in press, 1996.

Ziolkowski, R. W., and J. B. Judkins, Full-wave vector Maxwell equation modeling of the self-focusing of ultrashort optical pulses in a nonlinear Kerr medium exhibiting a finite response time, *J. Opt. Soc. Am. B Opt. Phys.*, *10*(2), 186–198, 1993a.

Ziolkowski, R. W., and J. B. Judkins, Applications of the nonlinear finite difference time domain (NL-FDTD) method to pulse propagation in nonlinear media: Self-focusing and linear-nonlinear interfaces, *Radio Sci.*, *28*(5), 901–911, 1993b.

Ziolkowski, R. W., and J. B. Judkins, Nonlinear finite-difference time-domain modeling of linear and nonlinear corrugated waveguides, *J. Opt. Soc. Am. B Opt. Phys.*, *11*(9), 1565–1575, 1994.

S. C. Hagness and A. Taflove, Department of Electrical Engineering and Computer Science, McCormick School of Engineering and Applied Science, Northwestern University, Evanston, IL 60208. (e-mail: s-hagness@nwu.edu; a-taflove@nwu.edu)

R. M. Joseph, Xerox Corporation, 800 Phillips Road, Webster, NY 14580. (e-mail: joseph@wrc.xerox.com)

(Received October 17, 1995; revised February 1, 1996; accepted February 7, 1996.)